



Ullah, Z., Kaczmarczyk, Ł. and Pearce, C.J. (2020) A three-dimensional hierarchic finite element-based computational framework for the analysis of composite laminates. *Composite Structures*, 293, 111968.

There may be differences between this version and the published version. You are advised to consult the publisher's version if you wish to cite from it.

<http://eprints.gla.ac.uk/208032/>

Deposited on: 7 May 2020

Enlighten – Research publications by members of the University of Glasgow  
<http://eprints.gla.ac.uk>

# A three-dimensional hierarchic finite element-based computational framework for the analysis of composite laminates

Z. Ullah<sup>a,1</sup>, L. Kaczmarczyk<sup>b</sup>, C. J. Pearce<sup>b</sup>

<sup>a</sup>*Advanced Composites Research Group, School of Mechanical and Aerospace Engineering, Queen's University Belfast, Ashby Building, Belfast, BT9 5AH, UK*

<sup>b</sup>*Glasgow Computational Engineering Centre, The James Watt School of Engineering, University of Glasgow, Glasgow, G12 8QQ, UK*

---

## Abstract

A three-dimensional hierarchic finite element-based computational framework is developed for the investigation of inter-laminar stresses and displacements in composite laminates of finite width. As compared to the standard finite elements, hierarchic finite elements allow to change the order of approximation both locally and globally without modifying the underlying finite element mesh leading to very accurate results for relatively coarse meshes. In this paper, both symmetric cross-ply and angle-ply laminates subjected to uniaxial tension are considered as test cases. Tetrahedral elements are used for the discretisation of laminates and uniform or global p-refinement is used to increase the order of approximation. Each ply within laminates is modelled as a linear-elastic, homogenous and orthotropic material. With increasing the order of approximation, the developed computational framework is able to capture the complex profiles of inter-laminar stresses and displacements very accurately. Results are compared with reference results from the literature and found in a very good agreement. The computational model is implemented in our in-house finite element software library Mesh-Oriented Finite Element Method (MoFEM). The computational framework has additional flexibility of high-performance computing and makes use of the state-of-the-art computational libraries including Portable, Extensible Toolkit for Scientific Computation (PETSc) and the Mesh-Oriented dataABase (MOAB).

*Keywords:* Hierarchic finite elements, Composites laminates, Free-edge effect, Inter-laminar stresses, Orthotropic material

---

<sup>1</sup>Corresponding author: z.ullah@qub.ac.uk (Z. Ullah)

## 1. Introduction

Due to their exceptional mechanical and chemical properties, fibre reinforced polymer (FRP) composites are used in a variety of industrial applications such as aerospace, automotive, marine, rail, energy, civil structures, biomedical, and oil and gas [1–3]. The successive stacking of unidirectional fibrous layers or woven fabric in combination with resin is used for the manufacturing of composites structures. The choice of fibre orientation in an individual layer or ply and the subsequent freedom in combining these layers provide designers with enormous flexibility to tailor the material properties in the desired directions. On the other hand, discontinuity/mismatch in the material properties across these layers leading to very large inter-laminar stresses, especially on approaching the free edges of laminates. In literature ([4, 5]), this is referred as free-edge or boundary-layer effect. The classical laminate theory (CLT) cannot predict these stresses. Due to very low inter-laminar normal and shear strengths, the free-edge effect can lead to the initiation of delamination and subsequent failure of composite laminates. Therefore, accurate calculations of the inter-laminar stresses are essential for the optimum design of composite structures.

In the literature, dated back to 1967, a variety of analytical and numerical methods have been proposed for the estimation of inter-laminar stresses and displacements in composite laminates of finite width subjected to a variety of loading scenarios. Due to their computational efficiency, analytical methods are often the first choice in assessing composite laminates [5–12]. Analytical methods make assumptions regarding the state of stress and strain in composite laminate and therefore can lead to erroneous results. For the detailed and accurate analysis of composite laminates, numerical methods are the obvious choice. Due to the numerical nature of this paper, a detailed review is provided of some of the available methods in the following. The scope of this paper allows to discuss a few methods from the literature and is therefore not claiming to be exhaustive. For the detailed review, readers are referred to specialised references, e.g. [5, 11, 12]. In [13], a finite difference-based numerical procedure was proposed. Symmetric laminates of finite width subjected to uniaxial tension were examined and inter-laminar stresses and displacements were calculated. Results were validated against the reference results from the literature. A two-dimensional finite element formulation was developed in [14] for the analysis of composite laminates under uniaxial tension. Constant strain triangular elements were used and Sky-line matrix storage was used to overcome the storage limitations. Inter-laminar normal and shear stresses were calculated for  $[0/90]_s$ ,  $[\pm 45]_s$  and  $[\pm 45/0/90]_s$  laminates, and were validated against the literature. A three-dimensional finite element formulation based on eight-node hexahedral elements was developed in [15]. Both symmetric cross-ply  $[90/0]_s$  and angle-ply  $[\pm 45]_s$  laminates subjected to uniaxial tension were considered as test cases. Distribution of inter-laminar stresses and displacements were calculated and compare with the results available in the literature. In addition to the free-edge effect, the severity of the end-edge effect was also

observed.

Due to its practical importance and industrial relevance, numerical modelling of composite laminates is currently an active research area. Over the last few years, researchers from around the globe have proposed a variety of new procedure for the efficient and accurate modelling of composite laminates. A finite element model based on the Multiparticle Model of Multilayered Materials (M4) was developed in [16]. The developed eight-node multi-particle element with  $5n$  degrees of freedom per node where  $n$  is the number of plies in composite laminates. The model was capable to capture the free-edge and other localised effects. An efficient and accurate procedure was presented for the recovery of inter-laminar stresses in composite laminates in [17]. The spurious oscillations were avoided by calculating these stresses directly at nodes without extrapolation from the super-convergent points [18]. Elasticity-based finite element formulation was developed in [19] and was used for the determination of free-edge effect in  $[\pm 25/90]_s$  T300/934 composite laminates. Numerical error estimation was used for the determination of optimal mesh size. Numerical and experimental studies were performed on a  $[+45, -45, 0]_s$  laminate subjected to uniaxial tension and a good correlation was found. A mixed-field multi-term extended Kantorovich method (MMEKM) was developed in [4] for the determination of the inter-laminar stresses in composites laminates subjected to uniaxial tension, bending, twisting and thermal loading. It was found that the solution accuracy increases with increasing the number of terms. In the case of laminated plain textile composites, a finite element-based approach was used in [20] for the investigation of the effect of layers' shifting on the inter-laminar and intra-laminar stresses. Two and four layer models with a variety of shifting configuration were studied. The laminates were trimmed at different locations for the investigation of the effect of boundaries on the inter-laminar stresses. It was found that the inter-laminar stresses depends on the layers' stacking configuration and shifting. Laminated composite plate with a circular hole in the middle subjected to compressive loading was modelled with both serial/parallel mixing theory and continuum damage model in [21].

A multi-scale model was used in [22] for modelling composite laminates. A macro-level model was used to capture the laminate stacking sequence and the global stress field for a given loading. The micro-level model was used for the prediction of stresses at the fibre and matrix level. The model was used to examine the  $[90/90]$  interface of a  $[25_n/-25_n/90_n]_s$  IM7/8552 carbon/epoxy laminate. Another multi-scale model was developed in [23] for the investigation of the effect of heterogeneity in the micro-structure for  $[\pm 45/0/90]_s$  laminate subjected to uniaxial tension. The  $0^\circ$  and  $90^\circ$  layers were modelled on the micro-level, i.e. random fibres within the polymer matrix. On the other hand, the  $\pm 45^\circ$  layers were modelled using homogenous and orthotropic materials. In [24], a global-local approach was used. The available software packages were used for the efficient design and analysis of composite structures on the global-level and the Carrera Unified Formulation (CUF) was used for the in-depth analysis of critical domains. In

[25], it was found that the maximum value of the displacement gradient is dependent on the orientation of the plies in the laminate. Symmetric laminates with varying stacking sequences and ply orientation were analysed and the displacement gradient was related to the inter-laminar stresses. In [26], a numerical approach was introduced to investigate generic laminated composites with arbitrary geometries. The model used a higher-order beam theory with only displacement unknown over the cross-section. Both conventional and wrap-around laminates were investigated using finite element analysis and inter-laminar stresses were calculated [27]. In [28], commercial finite element software, ANSYS, was used to study hybrid and non-hybrid composite laminates. Both carbon and glass fibres were used in the hybrid laminates. A coupled stress and energy criteria using finite fracture mechanics was used in [29]. The scale-boundary finite element technique was used as a numerical tool, which due to its semi-analytical nature reduces the numerical effort significantly as compared to standard finite element analysis.

In addition to mechanical loading, composite laminates subjected to temperature change were also investigated and results were presented in the form of temperature, stress and displacement distributions. For uniform temperature change, thermal stresses and displacements were calculated in composite laminates in [30]. The laminate-level homogenised or effective coefficients of thermal expansion were expressed in-term of the ply-level coefficients of thermal expansion. Similarly, a variational model was developed in [31] for the determination of the inter-laminar stresses and displacements for symmetric laminates subjected to thermo-mechanical loads. The stresses along the free-edge were divided into two parts, i.e. perturbed and unperturbed. The principle of minimum complementary energy is used to obtain optimal stress and displacement fields which exactly satisfy equilibrium, compatibility, boundary and continuity conditions. A plane strain finite element-based Quasi-2D (Q-2D) formulation was developed in [32] to determine the inter-laminar stresses and free-edge effects in composite laminates subjected to both uniaxial and thermal loading.

This paper presents a hierarchic finite element-based computational framework for the efficient and accurate investigation of inter-laminar stresses and displacements in composite laminates of finite width subjected to uniaxial tension. The hierarchic finite elements allow to change the order of approximation locally or globally without changing the underlying finite element mesh leading to very accurate results for relatively coarse meshes [33–38]. As compared to the standard finite element, in hierarchic finite elements high order shape functions are calculated from low order shape functions recursively and therefore maintain the continuity in the shape functions across the element in the case of localised p-refinement. The computational model is implemented in our in-house finite element software library, Mesh-Oriented Finite Element Method (MoFEM) [38]. MoFEM is tailored for the solution of multi-physics problems with arbitrary levels of approximation, different levels of mesh refinement and optimised for high-performance computing. The computational framework make use of the state-of-the-

art computational libraries including Portable, Extensible Toolkit for Scientific Computation (PETSc) [39–42] and the Mesh-Oriented datABase (MOAB) [43]. MoFEM has already been used for a variety of applications including multi-scale and multi-physics modelling of composite materials [3, 44, 45], stochastic finite element analysis of composite materials [46] and fracture modelling of nuclear graphite [47]. In this paper, tetrahedral elements are used for the discretisation of composite laminates and global or uniform p-refinement is used to improve the solution accuracy. Symmetric cross-ply  $[90/0]_s$  and angle-ply  $[\pm 45]_s$  laminates subjected to uniaxial tension are considered as test cases. Each ply within these laminates is modelled as a linear-elastic, homogenised and orthotropic material. The inter-laminar stresses and displacements are compared with the reference results from the literature.

This paper is organised as follows. A detailed description of the theoretical background and mathematical formulation of composite laminates are given in §2. The finite element implementation aspects based on hierarchic basis function is given in §3. The detailed regarding the finite element’s stiffness matrix, force vector, and displacement vector is given in §3.1. Moreover, numerical integration procedure for hierarchic finite elements is given in §3.2. Two numerical examples are given in §4 to validate the correct implementation and accuracy of the computational framework. The first numerical example is given in §4.1 consisting of an angle-ply  $[\pm 45]_s$  laminate while the second numerical example is given in §4.2 consisting of a cross-ply laminate. Finally, concluding remarks are given in §5.

## 2. Composites laminates

Consider a square symmetric laminate  $[\pm\theta]_s$  consisting of four plies each of thickness  $h$ , subjected to uniaxial strain  $\epsilon_0$  as shown in Figure 1. The global coordinate system  $xyz$  is also given in the same figure, where  $x$  and  $y$  are the laminate’s in-plane directions and  $z$  is its out-of-plane or through-the-thickness direction.  $2l$  is the length and width of the laminate in the in-plane direction. The strain  $\epsilon_0$  is applied to the two  $y$  faces. The local coordinate system of each ply is represented by 123, where 1, 2 and 3 are fibre, transverse and through-the-thickness directions respectively.  $\theta$  is the angle between the local and global coordinate systems. Each lamina within the laminate is modelled as a linear-elastic, homogenous and orthotropic material.

For each individual ply, the relationship between stresses and strains in Voigt notation is given

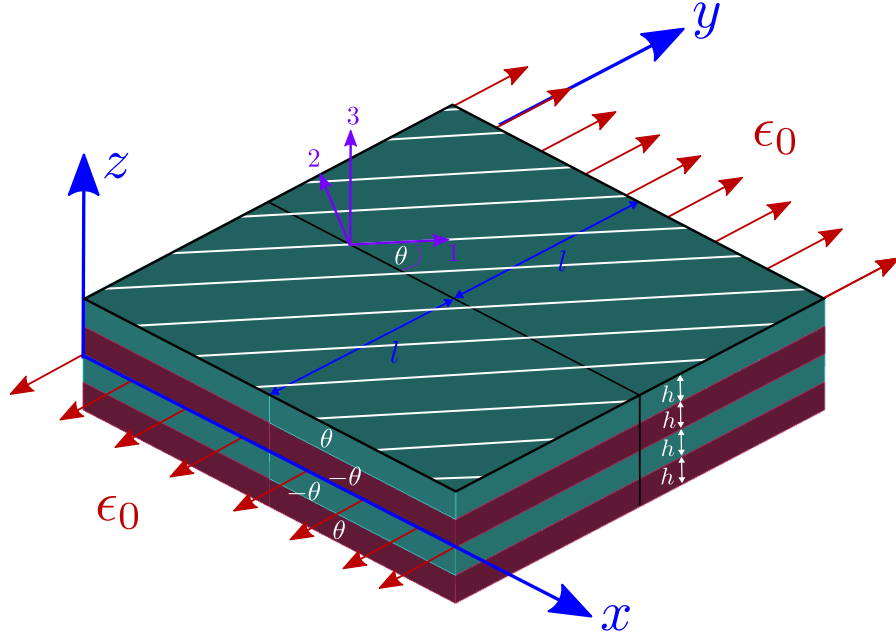


Figure 1: Geometry, boundary conditions and coordinate systems for composite laminate

as follows:

$$\begin{Bmatrix} \varepsilon_{11} \\ \varepsilon_{22} \\ \varepsilon_{33} \\ \gamma_{12} \\ \gamma_{23} \\ \gamma_{31} \end{Bmatrix} = \mathbf{S}_{123} \begin{Bmatrix} \sigma_{11} \\ \sigma_{22} \\ \sigma_{33} \\ \tau_{12} \\ \tau_{23} \\ \tau_{31} \end{Bmatrix}, \quad \text{where} \quad \mathbf{S}_{123} = \mathbf{C}_{123}^{-1}, \quad (1)$$

where  $\sigma_{11}$ ,  $\sigma_{22}$  and  $\sigma_{33}$  are normal stresses in the fibre, transverse and thickness directions respectively. Similarly,  $\varepsilon_{11}$ ,  $\varepsilon_{22}$  and  $\varepsilon_{33}$  are normal strains in fibre, transverse and thickness directions. Moreover,  $\tau_{12}, \tau_{23}, \tau_{31}$  and  $\gamma_{12}, \gamma_{23}, \gamma_{31}$  are shear stresses and strain respectively. Matrices  $\mathbf{S}_{123}$  and  $\mathbf{C}_{123}$  are ply-level compliance and stiffness matrices respectively. For an orthotropic material the compliance matrix  $\mathbf{S}_{123}$  is written as:

$$\mathbf{S}_{123} = \begin{bmatrix} \frac{1}{E_{11}} & -\frac{\nu_{21}}{E_{22}} & -\frac{\nu_{31}}{E_{33}} & 0 & 0 & 0 \\ -\frac{\nu_{12}}{E_{11}} & \frac{1}{E_{22}} & -\frac{\nu_{32}}{E_{33}} & 0 & 0 & 0 \\ -\frac{\nu_{13}}{E_{11}} & -\frac{\nu_{23}}{E_{22}} & \frac{1}{E_{33}} & 0 & 0 & 0 \\ 0 & 0 & 0 & \frac{1}{G_{12}} & 0 & 0 \\ 0 & 0 & 0 & 0 & \frac{1}{G_{23}} & 0 \\ 0 & 0 & 0 & 0 & 0 & \frac{1}{G_{31}} \end{bmatrix}, \quad (2)$$

where  $E_{11}$ ,  $E_{22}$  and  $E_{33}$  are the ply-level Young's moduli in the fibre, transverse and through-the-thickness directions respectively.  $\nu_{ij}$  and  $G_{ij}$  are the ply-level Poisson's ratio and shear

modulus respectively. Due to the symmetry of the compliance matrix

$$\frac{\nu_{21}}{E_{22}} = \frac{\nu_{12}}{E_{11}}, \quad \frac{\nu_{31}}{E_{33}} = \frac{\nu_{13}}{E_{11}}, \quad \frac{\nu_{32}}{E_{33}} = \frac{\nu_{23}}{E_{22}} \quad (3)$$

For the finite element analysis, a global compliance/stiffness matrix is required in the  $xyz$  coordinate system of laminate. The transformation of ply-level stiffness matrix  $\mathbf{C}_{123}$  from its local coordinate 123 to the laminate global coordinate  $xyz$  is given as:

$$\mathbf{C}_{xyz} = \mathbf{T}^{-1} \mathbf{C}_{123} \mathbf{T}^{-T}, \quad (4)$$

where  $\mathbf{C}_{xyz}$  is a transformed stiffness matrix in global coordinates  $xyz$  and  $\mathbf{T}$  is a transformation matrix and is given as:

$$\mathbf{T} = \begin{bmatrix} \cos^2 \theta & \sin^2 \theta & 0 & 0 & 0 & \sin 2\theta \\ \sin^2 \theta & \cos^2 \theta & 0 & 0 & 0 & -\sin 2\theta \\ 0 & 0 & 1 & 0 & 0 & 0 \\ 0 & 0 & 0 & \cos \theta & -\sin \theta & 0 \\ 0 & 0 & 0 & \sin \theta & \cos \theta & 0 \\ -\frac{1}{2} \sin 2\theta & \frac{1}{2} \sin 2\theta & 0 & 0 & 0 & \cos 2\theta \end{bmatrix}. \quad (5)$$

### 3. Implementation aspects of the hierarchic finite elements

A brief theoretical background and implementation aspects of the hierarchic finite elements is explained in the case of tetrahedral elements in this section. For further details and comprehensive review, readers are referred to specialised references, e.g. [33–38]. As compared to standard finite element, hierarchic finite elements allow to change the order of approximation both locally and globally without changing the underlying finite element mesh leading to very accurate results for relatively coarse meshes. Due to their hierarchic nature, these elements are considered as an ideal candidate for p-refinement. In the case of these elements, their high-order shape functions are obtained recursively from their low order shape functions and therefore preserving the continuity of the shape functions across the element boundaries. In addition to the linear shape functions associated with the four vertices of the tetrahedron, high order shape functions are added to its edges, faces and interior with increasing the order of approximation. Due to these additional shape functions, virtual degrees of freedom are assigned to edges, faces and interior for the approximation of the field variables. The continuity requirement for the shape functions associated with different spaces, e.g.  $H^1(\Omega)$ ,  $\mathbf{H}(\mathbf{curl}; \Omega)$ ,  $\mathbf{H}(\mathbf{div}; \Omega)$ , and  $L_2(\Omega)$  are different which is explained in [33]. In the following, the procedure to construct the shape functions for  $H^1(\Omega)$  space is discussed in detail.



Consider a one-dimensional reference interval  $I = [-1, 1]$  for the construction of hierarchic shape functions  $\{\phi_l : l = 0, 1, \dots\}$ . The shape functions associated with its vertices are the standard linear finite element shape functions, shown in Figure 2(b). The high order shape functions associated with increasing the order of approximation are constructed by combining these linear shape functions and some arbitrary polynomials  $\{\psi_l : l = 0, 1, \dots\}$  of degree  $l$ . There is no restriction on the choice of polynomials but Legendre polynomials are often used. Legendre polynomials of high order are obtained recursively from their low order counterparts. The equation for Legendre polynomial  $L_l$  of degree  $l$  is given as ([33]):

$$\begin{aligned} L_0(s) &= 1, & L_1(s) &= s, \\ L_{l+1}(s) &= \frac{2l+1}{l+1}sL_l(s) - \frac{l}{l+1}L_{l-1}(s), & l &= 1, 2, \dots \end{aligned} \quad (6)$$

Legendre polynomials is a special case of Gegenbauer polynomials with  $\alpha = \frac{1}{2}$ , which is given as:

$$\begin{aligned} \psi_0(s) &= 1, & \psi_1(s) &= 2\alpha s, \\ \psi_{l+1}(s) &= \frac{2(\alpha+l)}{l+1}s\psi_l(s) - \frac{2\alpha+l-1}{l+1}\psi_{l-1}(s), & l &= 1, 2, \dots \end{aligned} \quad (7)$$

The first seven Legendre polynomials, i.e. for  $l = 0, 1, \dots, 6$  over the domain  $s = [-1, 1]$  are shown in Figure 2(a). For a line, triangle and tetrahedron, the linear shape functions associated with their vertices are given as:

$$\begin{aligned} N_o &= 1 - \xi, & N_i &= \xi, & \text{Edge} \\ N_o &= 1 - \xi - \eta, & N_i &= \xi, & N_j = \eta, & \text{Triangle} \\ N_o &= 1 - \xi - \eta - \zeta, & N_i &= \xi, & N_j = \eta, & N_k = \zeta, & \text{Tetrahedron} \end{aligned} \quad (8)$$

Where  $\xi$ ,  $\eta$  and  $\zeta$  are the reference coordinates of the corresponding line, triangle and tetrahedron elements. With known linear shape functions (Equation (8)) and Gegenbauer/Legendre polynomials (Equations (6) and (7)), the high order shape functions for edges  $e = [o, i]$ , faces  $f = [o, i, j]$  and interior of the tetrahedron  $t = [o, i, j, k]$  are given as:

$$\begin{aligned} \phi_l^e &= \beta_{oi}\psi_l(\hat{\zeta}_{oi}), & 0 \leq l \leq p-2 & \text{Edge} \\ \phi_{lm}^f &= \beta_{oij}\psi_l(\hat{\zeta}_{oi})\psi_m(\hat{\zeta}_{oj}), & 0 \leq l, m, \quad l+m \leq p-3 & \text{Face} \\ \phi_{lmn}^t &= \beta_{oijk}\psi_l(\hat{\zeta}_{oi})\psi_m(\hat{\zeta}_{oj})\psi_n(\hat{\zeta}_{ok}), & 0 \leq l, m, n \quad l+m+n \leq p-4 & \text{Tetrahedron Interior} \end{aligned} \quad (9)$$

where  $\beta_{oi} = N_o N_i$ ,  $\beta_{oij} = N_o N_i N_j$ ,  $\beta_{oijk} = N_o N_i N_j N_k$ ,  $\hat{\zeta}_{oi} = N_i - N_o$ ,  $\hat{\zeta}_{oj} = N_j - N_o$  and  $\hat{\zeta}_{ok} = N_k - N_o$ . Moreover,  $p$  is the user-defined order of approximation for the finite element analysis. Linear ( $N_0, N_1$ ) and high order shape functions ( $\phi_l^e$ ) for an edge ( $e = oi$ ) are given in Figure 2(b). For the first order of approximation, i.e.  $p = 1$ , there will be only linear

shape functions  $N_0$  and  $N_1$  associated with its vertices. For  $p = 2$ , in addition to the linear shape functions  $N_0$  and  $N_1$ , we will have one high order shape function, i.e.  $\phi_0^{oi}$ . All the shape functions for  $p = 7$  including linear and high order, i.e.  $\phi_l^{oi}, l = 0, 1, \dots, 5$  are shown in Figure 2(b).

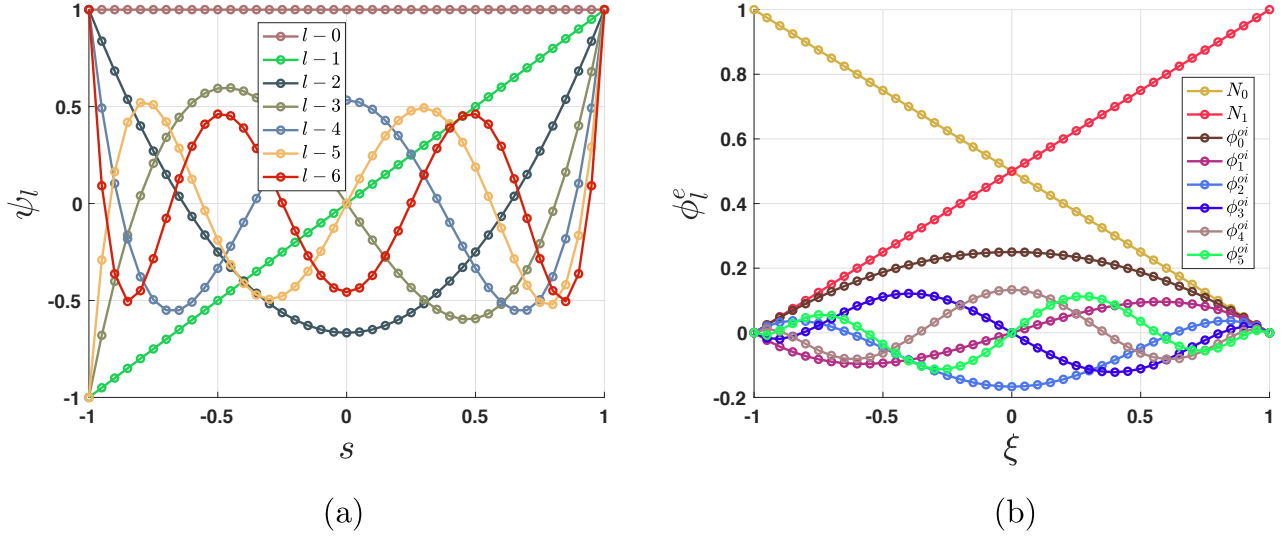


Figure 2: Legendre polynomials and corresponding linear and high-order shape functions for an edge

For a triangular element, linear shape functions  $N_i$ ,  $N_j$  and  $N_k$  for its vertices  $i$ ,  $j$  and  $k$  are shown in Figures 3(a), 3(b) and 3(c) respectively. These are standard linear shape functions for a triangular element. For first order of approximation, i.e.  $p = 1$ , we will have only linear shape functions and therefore degrees of freedom will be associated with vertices only. For second order of approximation, i.e.  $p = 2$ , in addition to the linear shape functions, we will have one quadratic shape function  $\phi_0^e$  associated with each edge of the triangle. Therefore, degrees of freedom will be associated with it vertices and edges. The quadratic shape functions, i.e.  $\phi_0^{oi}$ ,  $\phi_0^{oj}$  and  $\phi_0^{ij}$  for the edges  $oi$ ,  $oj$  and  $ij$  are shown in Figure 4(a), 4(b) and 4(c) respectively. Similarly, for  $p = 7$ , six degrees of freedom will be associated with each edge of a triangle. These high order shape functions  $\phi_l^{oi}$ ,  $l = 0, 1, \dots, 5$  for  $p = 7$  are shown in Figure 5. For the face of triangle  $oij$ , there are no shape functions and associated degrees of freedom for the first two order of approximations, i.e.  $p = 1, 2$ . For  $p = 3$ , there will be only one shape function  $\phi_{00}^{oij}$  associated with the face  $oij$  and there will be only one associated degree of freedom. The ten shape function associated with  $p = 6$ , i.e.  $\phi_{lm}^f$  are shown in Figure 6. It is trivial exercise to extend the aforementioned explanation for the construction of shape functions to a tetrahedron element and is therefore omitted here.

The number of degrees of freedom associated with these high order shape functions for each edge ( $\text{DOF}_e$ ), face ( $\text{DOF}_f$ ) and interior of the tetrahedron ( $\text{DOF}_t$ ) depend on the order of

approximation  $p$  and are given as:

$$\text{DOF}_v = 1, \quad \text{DOF}_e = p - 1, \quad \text{DOF}_f = \frac{(p-2)(p-1)}{2}, \quad \text{DOF}_t = \frac{(p-3)(p-2)(p-1)}{6} \quad (10)$$

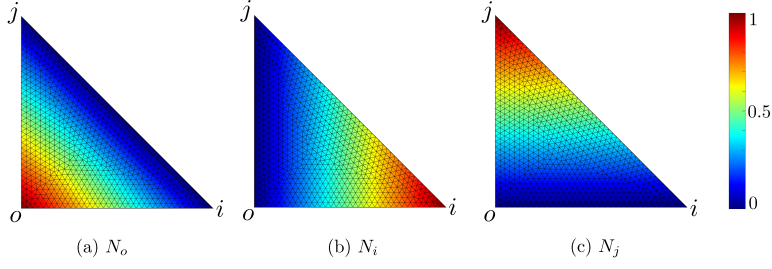


Figure 3: Linear shape functions  $N_0$ ,  $N_1$  and  $N_3$  for the vertices of a triangular element with  $p = 1$

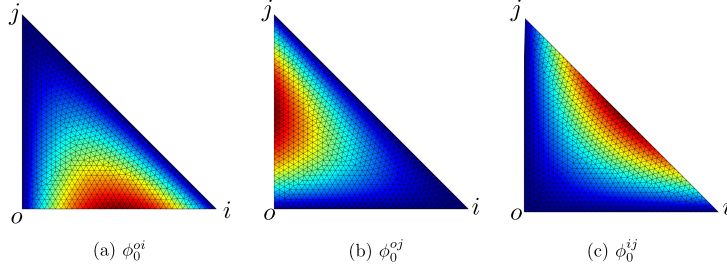


Figure 4: Quadratic shape functions  $\phi_0^e$  for the edges  $oi$ ,  $oj$  and  $ij$  of a triangular element with  $p = 2$

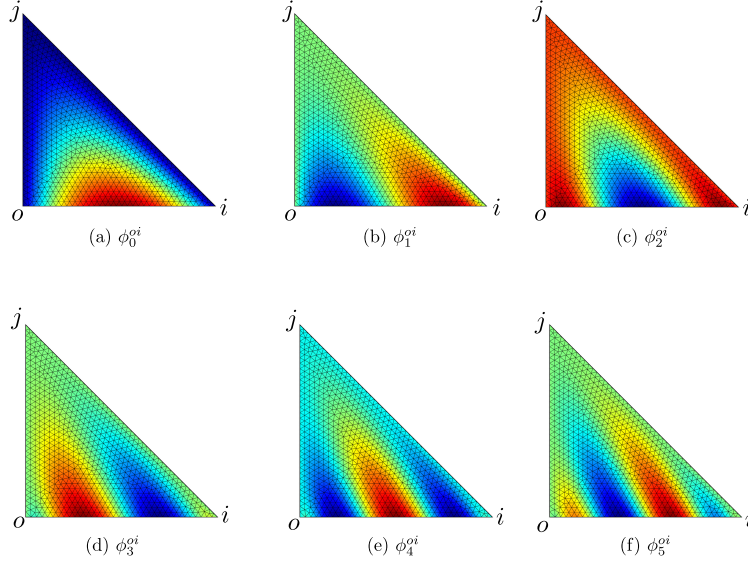


Figure 5: High order shape functions  $(\phi_l^e)$  for the edge  $oi$  of a triangular element with  $2 \leq p \leq 7$

### 3.1. Assembly of stiffness matrix

The final discretised system of equations in the case of finite element analysis is given as:

$$\mathbf{K}\mathbf{u} = \mathbf{f}, \quad (11)$$

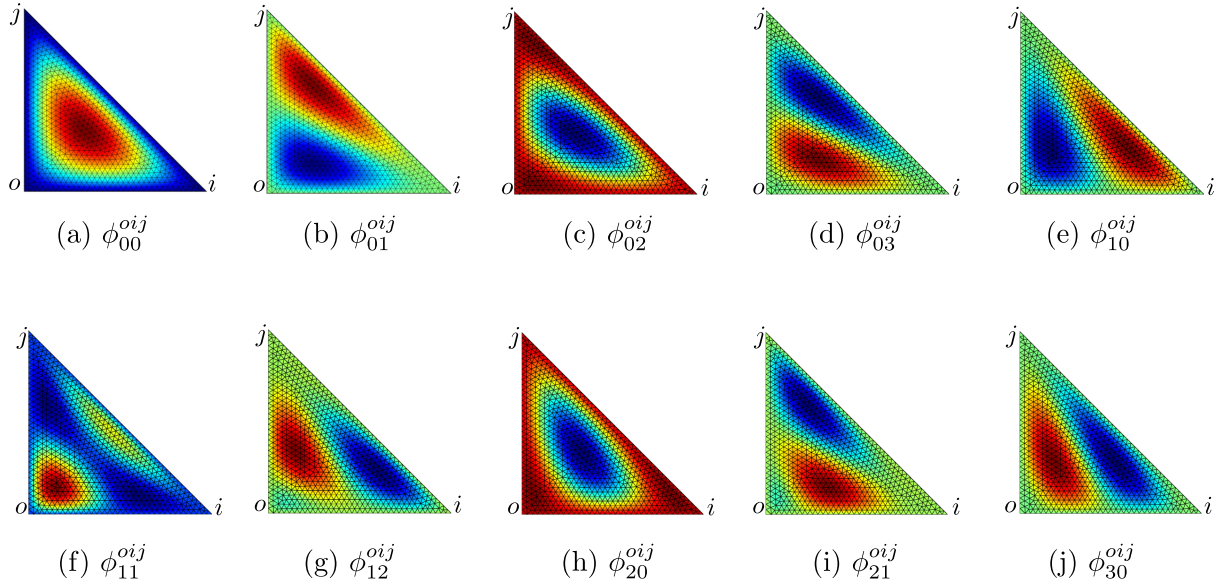


Figure 6: High order shape functions ( $\phi_{lm}^f$ ) for the face  $oij$  of a triangular element with  $p = 6$

where  $\mathbf{K}$  is the global stiffness matrix,  $\mathbf{f}$  is the right hand side force vector and  $\mathbf{u}$  is the unknown degrees of freedom. Matrix  $\mathbf{K}$  is given as:

$$\mathbf{K} = \sum_{j=1}^{n_e} \int_{\Omega_j} \mathbf{B}^T \mathbf{C}_{xyz} \mathbf{B} d\Omega_j = \sum_{j=1}^{n_e} \mathbf{K}_j, \quad (12)$$

Here  $\mathbf{K}_j$  is the element stiffness matrix,  $\mathbf{C}_{xyz}$  is the transformed  $6 \times 6$  stiffness matrix for the orthotropic material (fully explained in §2),  $n_e$  is the total number of elements and  $\sum_{j=1}^{n_e}$  represents the standard finite element assembly operation. The size of matrix  $\mathbf{B}$  and consequent size of matrix  $\mathbf{K}_j$  depends on the order of approximation. For the first order of approximation, i.e.  $p = 1$ , matrix  $\mathbf{B}$  for tetrahedral element consists of contribution from its four vertices only and is given as:

$$\mathbf{B}_{(6 \times 12)} = \begin{bmatrix} \frac{\partial N_1}{\partial x} & 0 & 0 & \dots & \frac{\partial N_4}{\partial x} & 0 & 0 \\ 0 & \frac{\partial N_1}{\partial y} & 0 & \dots & 0 & \frac{\partial N_4}{\partial y} & 0 \\ 0 & 0 & \frac{\partial N_1}{\partial z} & \dots & 0 & 0 & \frac{\partial N_4}{\partial z} \\ \frac{\partial N_1}{\partial y} & \frac{\partial N_1}{\partial x} & 0 & \dots & \frac{\partial N_4}{\partial y} & \frac{\partial N_4}{\partial x} & 0 \\ 0 & \frac{\partial N_1}{\partial z} & \frac{\partial N_1}{\partial y} & \dots & 0 & \frac{\partial N_4}{\partial z} & \frac{\partial N_4}{\partial y} \\ \frac{\partial N_1}{\partial z} & 0 & \frac{\partial N_1}{\partial x} & \dots & \frac{\partial N_4}{\partial z} & 0 & \frac{\partial N_4}{\partial x} \end{bmatrix}, \quad (13)$$

where the term  $(6 \times 12)$  represents the size of matrix  $\mathbf{B}$  for tetrahedral element. The sizes of vectors  $\mathbf{f}$  and  $\mathbf{u}$  also dependent on the user-defined order of approximation. For  $p = 1$ , element-level vectors  $\mathbf{f}_j$  and  $\mathbf{u}_j$  will consists of contribution of only vertices. Both  $\mathbf{f}_j$  and  $\mathbf{u}_j$  will have size of  $(12 \times 1)$ . For the second order of approximation, i.e.  $p = 2$ , in addition to the degrees of freedom associated with vertices, we will have three degrees of freedom associated

with each edge. For  $p = 2$ , matrix  $\mathbf{B}$  is written as:

$$\mathbf{B}_{(6 \times 30)} = \begin{bmatrix} \frac{\partial N_1}{\partial x} & 0 & 0 & \dots & \frac{\partial N_4}{\partial x} & 0 & 0 & \frac{\partial \phi_0^{e1}}{\partial x} & 0 & 0 & \dots & \frac{\partial \phi_0^{e6}}{\partial x} & 0 & 0 \\ 0 & \frac{\partial N_1}{\partial y} & 0 & \dots & 0 & \frac{\partial N_4}{\partial y} & 0 & 0 & \frac{\partial \phi_0^{e1}}{\partial y} & 0 & \dots & 0 & \frac{\partial \phi_0^{e6}}{\partial y} & 0 \\ 0 & 0 & \frac{\partial N_1}{\partial z} & \dots & 0 & 0 & \frac{\partial N_4}{\partial z} & 0 & 0 & \frac{\partial \phi_0^{e1}}{\partial z} & \dots & 0 & 0 & \frac{\partial \phi_0^{e6}}{\partial z} \\ \frac{\partial N_1}{\partial y} & \frac{\partial N_1}{\partial x} & 0 & \dots & \frac{\partial N_4}{\partial y} & \frac{\partial N_4}{\partial x} & 0 & \frac{\partial \phi_0^{e1}}{\partial y} & \frac{\partial \phi_0^{e1}}{\partial x} & 0 & \dots & \frac{\partial \phi_0^{e6}}{\partial y} & \frac{\partial \phi_0^{e6}}{\partial x} & 0 \\ 0 & \frac{\partial N_1}{\partial z} & \frac{\partial N_1}{\partial y} & \dots & 0 & \frac{\partial N_4}{\partial z} & \frac{\partial N_4}{\partial y} & 0 & \frac{\partial \phi_0^{e1}}{\partial z} & \frac{\partial \phi_0^{e1}}{\partial y} & \dots & 0 & \frac{\partial \phi_0^{e6}}{\partial z} & \frac{\partial \phi_0^{e6}}{\partial y} \\ \frac{\partial N_1}{\partial z} & 0 & \frac{\partial N_1}{\partial x} & \dots & \frac{\partial N_4}{\partial z} & 0 & \frac{\partial N_4}{\partial x} & \frac{\partial \phi_0^{e1}}{\partial z} & 0 & \frac{\partial \phi_0^{e1}}{\partial x} & \dots & \frac{\partial \phi_0^{e6}}{\partial z} & 0 & \frac{\partial \phi_0^{e6}}{\partial x} \end{bmatrix}, \quad (14)$$

where  $\phi_0^{e_i}$  with  $i = 1, 2, \dots, 6$  are quadratic shape functions associated with each edge of the tetrahedron. Similarly, the size of vectors  $\mathbf{f}_j$  and  $\mathbf{u}_j$  will change to be  $(30 \times 1)$ . For higher order, i.e.  $p > 2$ , sizes of matrix  $\mathbf{B}_j$ , and vectors  $\mathbf{f}_j$  and  $\mathbf{u}_j$  will change according to the addition of new hierarchic shape functions.

### 3.2. Numerical Integration

The standard integration procedure of a function  $f$  over domain  $\Omega$  is shown as:

$$\int_{\Omega} f d\Omega = \sum_{j=1}^{n_e} \int_{\Omega_j} f d\Omega_j = \sum_{j=1}^{n_e} \sum_{k=1}^{n_g} \omega_k f(\mathbf{x}_k) |\mathbf{J}|, \quad (15)$$

where  $\Omega_e$  is domain of an individual element and  $n_e$  is the total number of element, i.e.  $\Omega = \sum_{j=1}^{n_e} \Omega_j$ .  $n_g$  is the number of integration points in an element. Moreover,  $\mathbf{x}_k = [x_k, y_k, z_k]^T$  are the spacial coordinate of integration point,  $\omega_k$  and  $|\mathbf{J}|$  are spacial positions, weight and jacobian associated with an integration point  $k$ . The total number and their corresponding position of integration points are essential for the accuracy of numerical results. For standard finite elements, numerical integration is well documented but literature is very limited in the case of hierarchic finite elements. The number of integration points and their corresponding position are selected accordance to Grundmann and Moller integration rule [34], i.e.

$$n_g = \frac{n!}{l!(n-l)!}, \quad n = d + l + 1, \quad (16)$$

where  $l$  is the degree of polynomial and  $d = 1, 2$ , or  $3$  is the dimensionality of problem.

## 4. Numerical Examples

Two numerical examples are presented now to demonstrate the correct implementation and performance of the developed computational framework. The first numerical example consists of

a symmetric angle-ply laminate  $[\pm 45]_s$  and the second numerical example consists of symmetric cross-ply laminate  $[90/0]_s$ .

#### 4.1. Angle-ply laminate

The geometry, boundary conditions and coordinate system for an angle-ply laminate is shown in Figure 7. A strain of  $\epsilon_0$  is applied to its  $y$ -faces. The boundary conditions on faces  $z = \pm 2h$  is represented as  $\sigma_{zz} = 0$ ,  $\sigma_{zx} = 0$ ,  $\sigma_{zy} = 0$ . On the faces  $x = 0$  and  $x = 2l$ , boundary conditions are represented as  $\sigma_{xx} = 0$ ,  $\sigma_{xy} = 0$ ,  $\sigma_{xz} = 0$ . Similarly, on the faces  $y = 0$  and  $y = 2l$ , boundary conditions are represented as  $\sigma_{yx} = 0$ ,  $\sigma_{yz} = 0$ . Angle ply laminate is symmetric only with respect to  $xy$  plane and therefore half of the laminate is modelled. In this case symmetry boundary conditions, i.e.  $u_z = 0$  is applied to the face with  $z = 0$ . Displacement  $u_y = 0$  is applied to face with  $y = 0$  and  $u_y = 2l\epsilon_0$  is applied to face with  $y = 2l$ . Faces with  $x = 0$  and  $x = 2l$  are free-edges. In this paper, dimensions of the laminate is chosen as  $h = 0.25$ ,  $l = 8h$  and the applied strain is chosen to be  $\epsilon_0 = 10^{-6}$ . The material properties used are  $E_{11} = 20 \times 10^6$ ,  $E_{22} = E_{33} = 2.1 \times 10^6$ ,  $G_{12} = G_{13} = G_{23} = 0.85 \times 10^6$ ,  $\nu_{12} = \nu_{13} = \nu_{23} = 0.21$  all in compatible units. Here 1, 2 and 3 represent the fibre, transverse and through-the-thickness directions respectively. Similar geometrical parameters and material properties were also used in [13–15]. Results are compared with the reference results from the above mentioned references. Mesh for this problem is shown in Figure 8 consisting of 22,938 tetrahedral elements and 6,325 nodes.

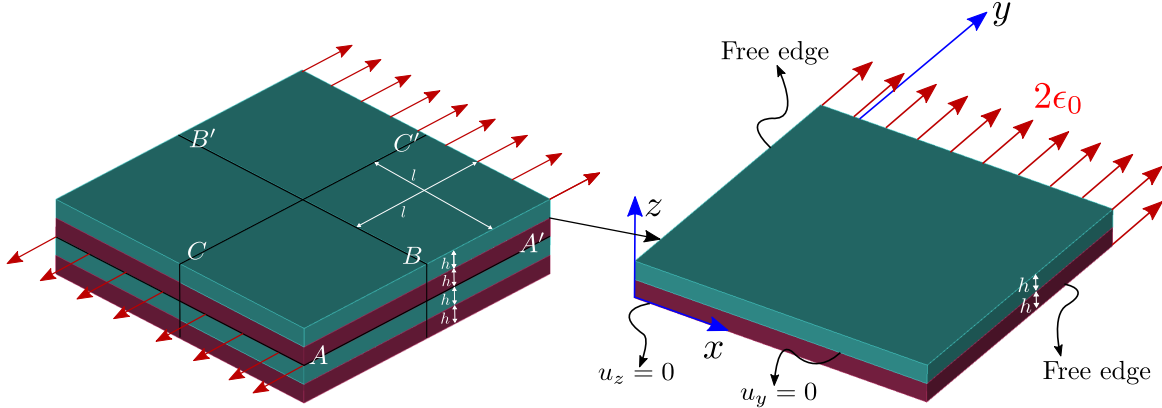


Figure 7: Geometry, boundary conditions and coordinate system for the angle-ply laminate

Distribution of inter-laminar in-plane stresses, i.e.  $\sigma_{xy}$  and  $\sigma_{yy}$  at  $y = l$ ,  $z = h$  versus  $x/l$  (along the green arrow), are shown in Figure 9. Results obtained with the current computational framework are compared with the ones from [15] and found in a very good agreement. Five orders of approximation ranging from order-1 to order-5, i.e.  $p = 1, 2, \dots, 5$  are used in the analysis. For both  $\sigma_{xy}$  and  $\sigma_{yy}$ , highest values of the stresses occur just before the free-edges (faces with  $x = 0$  and  $x = 2l$ ) and then converge to finite values at free-edges. The highest



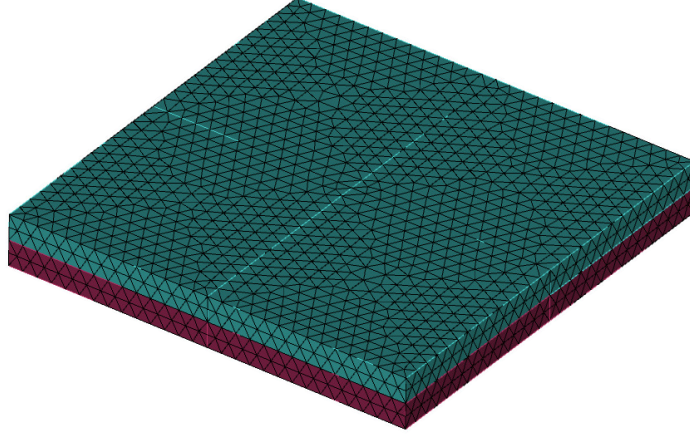


Figure 8: Mesh for the angle-ply laminate

values of these stresses increase with increasing the order of approximation. The difference is very high between the first and second order of approximation but converge to fixed values with further increasing the approximation order. The stress distribution is almost the same for the fourth and fifth orders of approximation. For  $x/l < 0.6$ , both  $\sigma_{xy}$  and  $\sigma_{yy}$  converge to values calculated by the classical laminate theory ([13]). Although, a very coarse mesh is used for the laminate discretisation but very accurate results are obtained with higher approximation orders.

Distribution for the inter-laminar out-of-plane stresses, i.e.  $\sigma_{zz}$ ,  $\sigma_{xz}$  and  $\sigma_{yz}$  versus  $x/l$  at  $y = l, z = h$  are shown in Figure 10. At  $x/l = 0$  the out-of-plane stresses are zero but on approaching the free-edges, i.e.  $x/l = 1$ , these stresses approaches singularity. In all these cases increasing the order of approximation improves the solution accuracy. As expected, the higher order of approximation lead to higher values of stresses at the free-edges. It is obvious from these plots that the free-edge effect is very localised. Finally, the distribution of displacement  $u_x$  versus  $y$  at  $z = h$  at three different locations, i.e.  $x = 0$ ,  $x = 2$  and  $x = 4$  are shown in Figure 11. The profile for  $u_x$  at  $x = 0$  is the mirror image of the  $u_x$  profile at  $x = 4$ . Displacement  $u_x$  are validated against the results from [15]. Displacement profiles at all three locations are in a very good agreement with the reference results. It is interesting to see that  $u_x$  versus  $y$  is not constant but give very complicated profiles. By changing the order of approximation from first order to second order, there is a big difference in the  $u_x$  versus  $y$  profile but the results converge with increasing the order of approximation. Results obtained with fourth and fifth orders of approximation almost coincide with each other.

#### 4.2. Cross-ply laminate

In this numerical example, boundary conditions and material properties are the same as in the previous numerical example. Due to symmetry about  $x$ -,  $y$ - and  $z$ -axis, only one-eighth of the

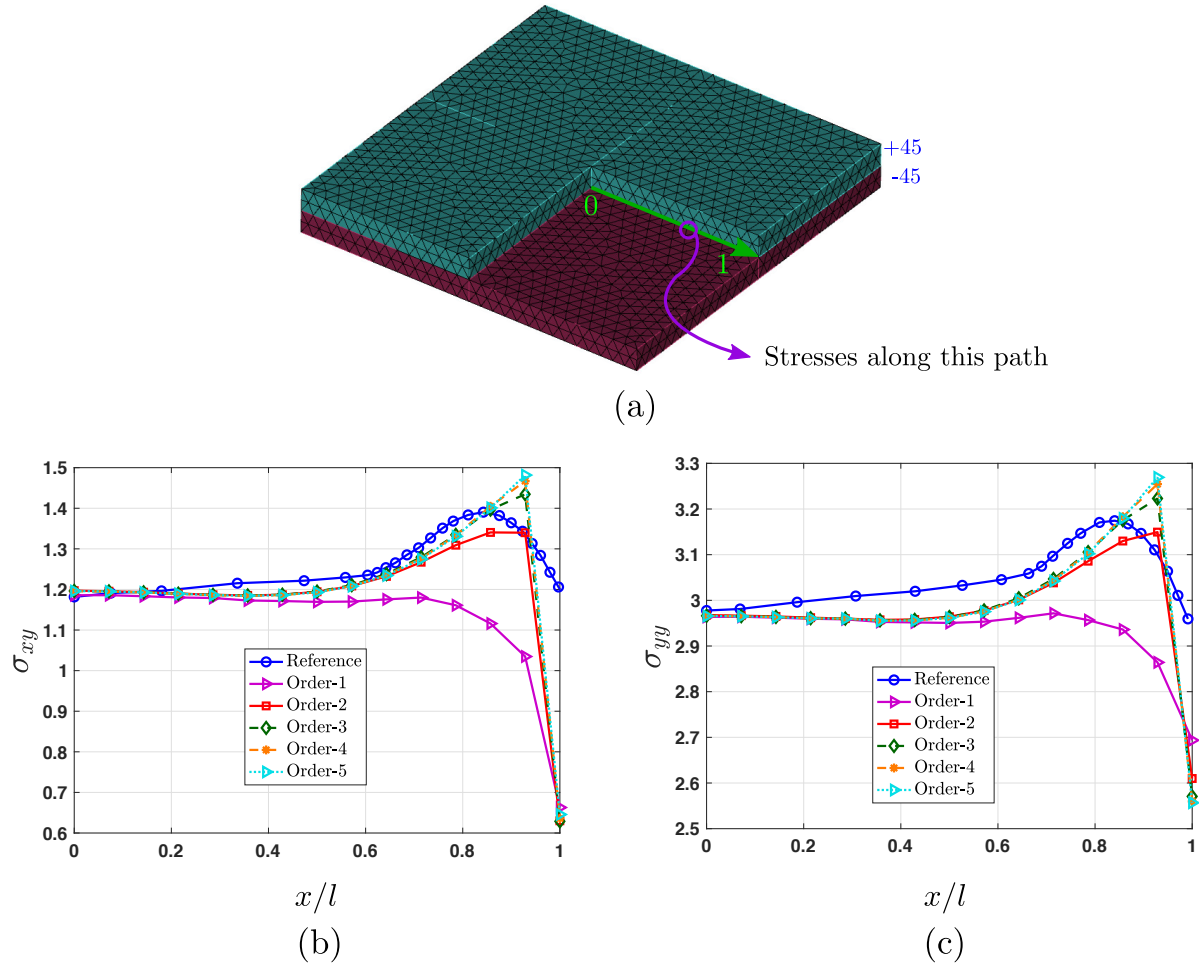


Figure 9: Inter-laminar in-plane stresses, i.e.  $\sigma_{xy}$  and  $\sigma_{yy}$  versus  $x/l$  at  $y = l, z = h$  for the angle-ply laminate

laminate is analysed as shown in Figure 12. For this numerical example, the global coordinate system is also shown in the same figure. Symmetry boundary conditions are applied to the three faces at  $x = 0$ ,  $y = 0$  and  $z = 0$ . Displacement of  $u_y = l\epsilon_0$  is applied to face with  $y = l$  and face with  $x = l$  is a free edge. Mesh for this problem is shown in Figure 13 consisting of 24,105 tetrahedral elements and 5,252 nodes.

Distribution of the inter-laminar out-of-plane stresses, i.e.  $\sigma_{zz}$  and  $\sigma_{yz}$  versus  $x/l$  are shown in Figure 14. At  $y = 0$  and  $z = 0$ ,  $\sigma_{zz}$  is shown in Figure 14(b). Two laminate types, i.e.  $(90/0)_s$  and  $(0/90)_s$  are considered in this case. These stresses increase rapidly on approaching the free-edge (at  $x/l = 1$ ) of the laminate. Results were compared with reference results from [14] and found in a very good agreement. Due to a very dense mesh near the free edge, results almost coincide with each other for all orders of approximation. For both  $(90/0)_s$  and  $(0/90)_s$ ,  $\sigma_{zz}$  converges to a finite value at the free-edge. In addition to the opposite sign of  $\sigma_{zz}$  for both  $(90/0)_s$  and  $(0/90)_s$ , there is also a noticeable difference in their magnitude at the free-edge. The  $\sigma_{zz}$  versus  $x/l$  at  $y = 0$  and  $z = h$  for both  $(90/0)_s$  and  $(0/90)_s$  laminates are shown in



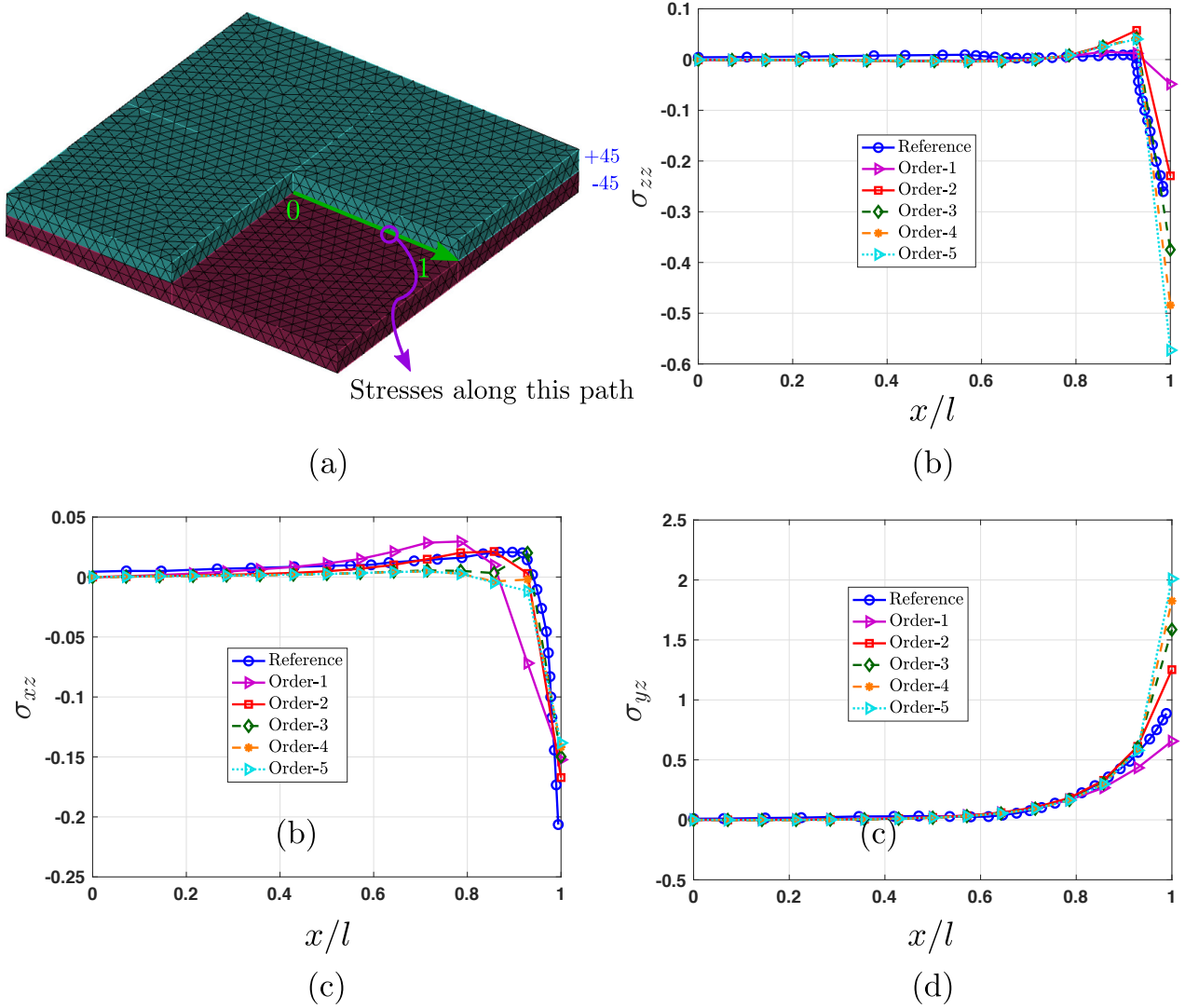


Figure 10: Inter-laminar out-of-plane stresses, i.e.  $\sigma_{zz}$ ,  $\sigma_{xz}$  and  $\sigma_{yz}$  versus  $x/l$  at  $y = l, z = h$  for the angle-ply laminate

Figure 14(c). Current results are compared with the reference results from [14] and are in a very good agreement. In this case, for  $(0/90)_s$  laminate,  $\sigma_{zz}$  behave very differently as compared to the  $(90/0)_s$  laminate. The  $\sigma_{zz}$  for  $(0/90)_s$  changes very rapidly on approaching the free-edge and leads to stress singularity. On the other hand, the stress  $\sigma_{zz}$  for  $(90/0)_s$  is relatively low. Although, the distribution of  $\sigma_{zz}$  predicted by the three orders of approximation, i.e.  $p = 1, 2, 3$  are in a very good agreement, but their magnitudes at the free-edges increase with increasing the order of approximation.

The distribution of inter-laminar out-of-plane shear stress  $\sigma_{yz}$  versus  $x/l$  at  $y = 0, z = h$  is shown in Figure 14(c) for both  $(90/0)_s$  and  $(0/90)_s$  laminates. This stress is also considered to be significant and can initiate delamination ([14]). For both  $(90/0)_s$  and  $(0/90)_s$  laminates,

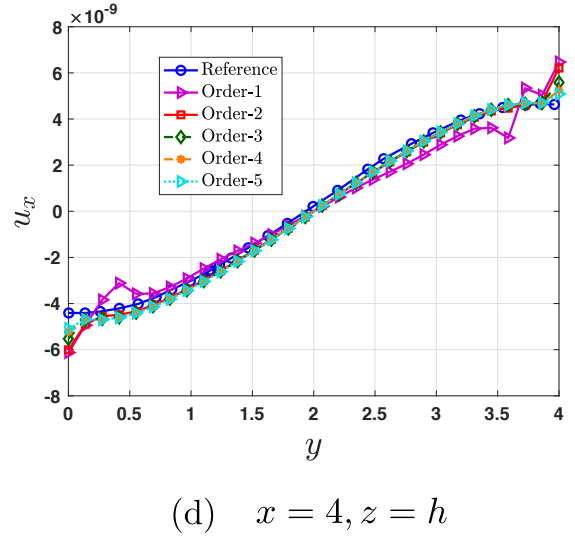
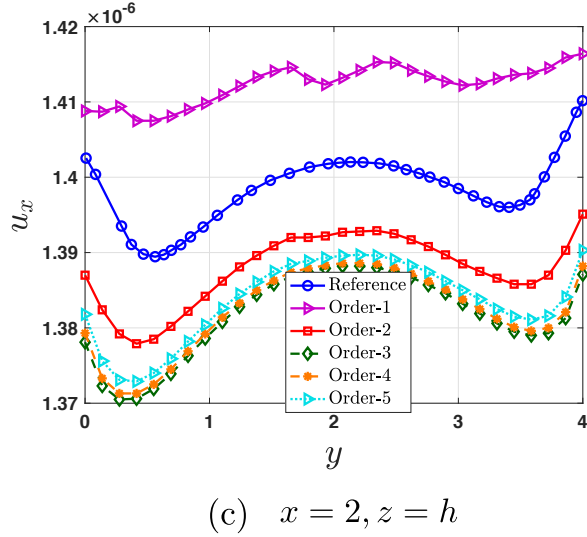
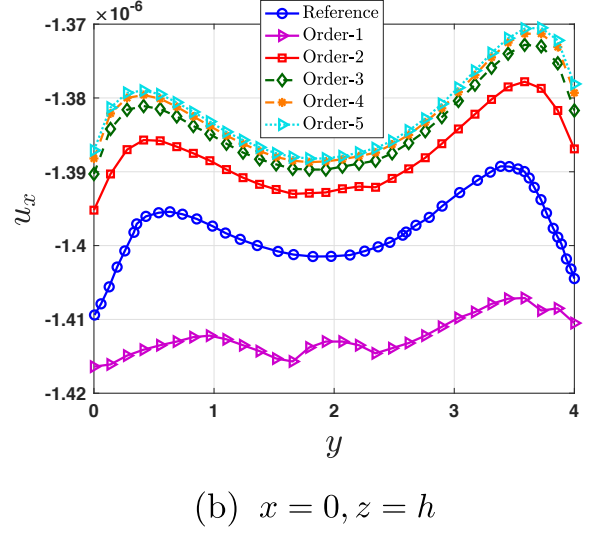
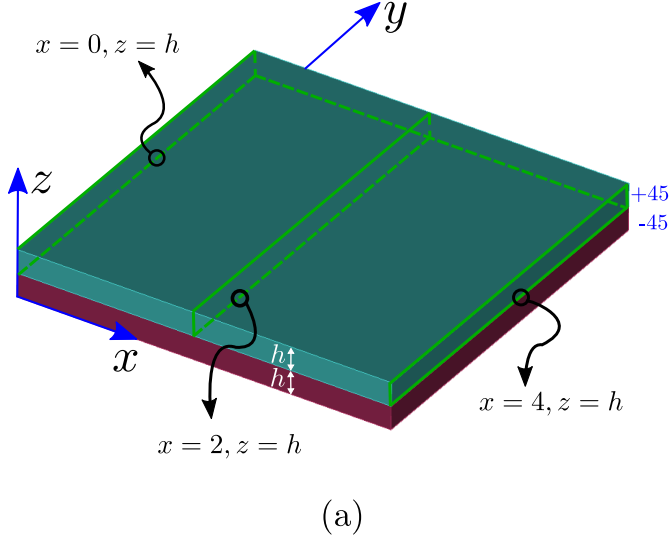


Figure 11: Displacement  $u_x$  versus  $y$  at  $z = h$  at locations  $x = 0$ ,  $x = 2$  and  $x = 4$  for the angle-ply laminate

the values of  $\sigma_{yz}$  increase initially and then decreases on approaching the free-edges. In this case, the effect of changing the order of approximation is clearly visible. For the first order of approximation, i.e.  $p = 1$ ,  $\sigma_{yz}$  fluctuate and is not in a very good agreement with the reference results from [14], especially at  $0.8 \leq x/l \leq 1$ . At the centre of the laminate, these stresses approach zero.

## 5. Concluding remarks

A three-dimensional computational framework based on hierarchic finite elements is presented for the analysis composite laminates. These elements allow changing the order of approximation globally or locally without changing the underlying finite element mesh leading to very

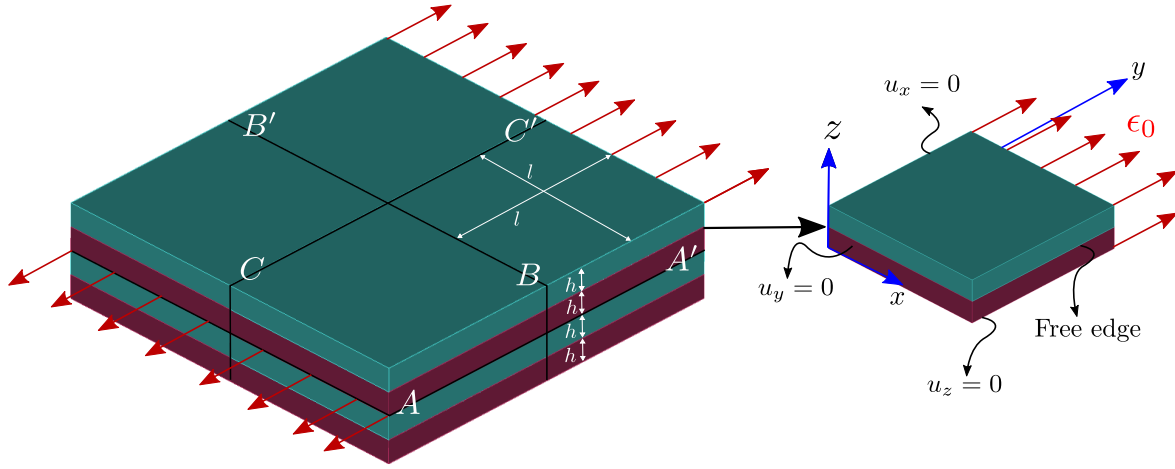


Figure 12: Geometry, boundary conditions and coordinate system for the cross-ply laminate

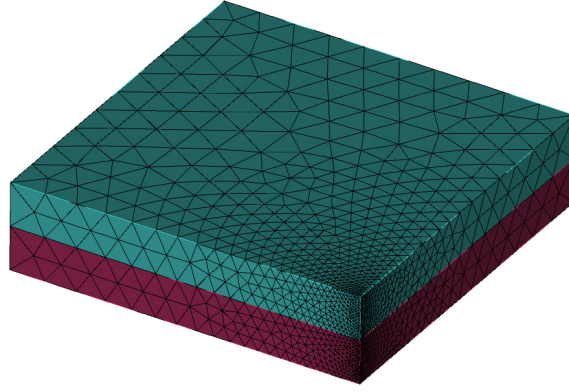


Figure 13: Mesh for the cross-ply laminate

accurate results for relatively coarse meshes. The correct implementation of the computational framework is validated with symmetric cross-ply  $[90/0]_s$  and angle-ply  $[\pm 45]_s$  composite laminates. Each ply within the laminate is modelled as a linear-elastic, homogenous and orthotropic material. Due to its symmetry about the  $z$ -axis, half of the laminate is modelled in the case of angle-ply laminate while only one-eighth of the laminate is modelled in the case of cross-ply laminate due to its symmetry about  $x$ ,  $y$  and  $z$ -axis. For the angle-ply laminate, five orders of approximation, i.e.  $p = 1, 2, \dots, 5$  are used while three orders of approximation are used for the cross-ply laminate. Both in-plane and out-of-plane inter-laminar stresses are plotted from the centre of laminates to their free-edges. For the angle-ply laminate, displacement  $u_x$  at  $z = h$  is also plotted against  $y$  at three different locations along  $x$ -axis, i.e.  $x = 0$ ,  $x = 2$  and  $x = 4$ . For the angle-ply laminate, in-plane stresses  $\sigma_{xy}$  and  $\sigma_{yy}$  are finite at its centre and approaches the values predicted by the classical laminate theory. The maximum values for these stresses occur just before the free edges and then converge to finite values at the free-edges. The out-of-plane normal ( $\sigma_{zz}$ ) and shear ( $\sigma_{xz}$  and  $\sigma_{yz}$ ) inter-laminar stresses are zero at the centre of the laminate but approach singularity at the free-edges. These results of the inter-laminar stresses and

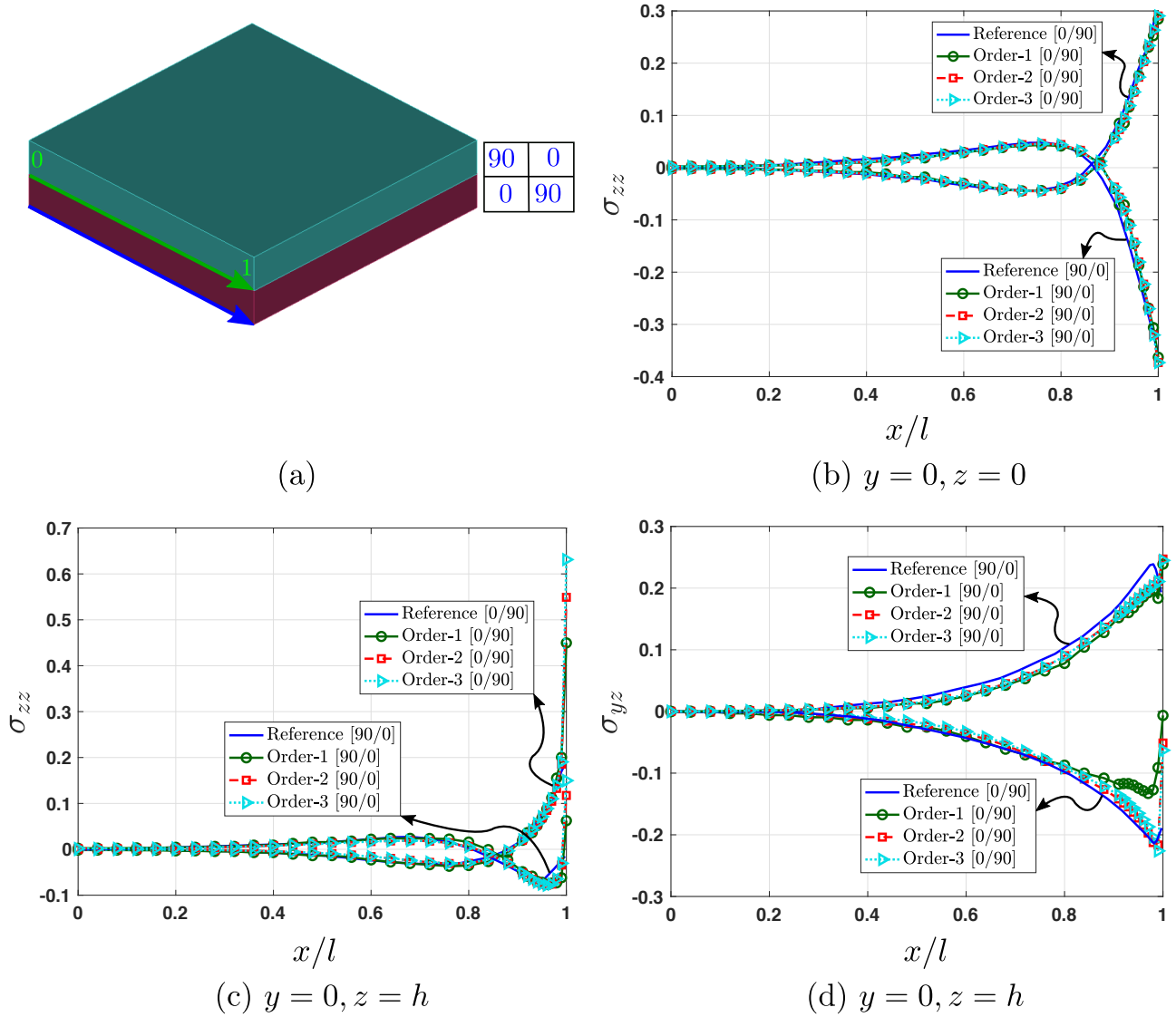


Figure 14: Inter-laminar out-of-plane stresses, i.e.  $\sigma_{zz}$  and  $\sigma_{yz}$  versus  $x/l$  at  $y = 0$  and  $z = 0, h$  for the cross-ply laminate

displacements are compared with the available results from the literature. At the centre of the laminates, all the approximation orders used in this paper give very accurate results due to the smoothness of stresses but start to deviate on approaching the free edges. At the free-edges, the use of lower orders of approximation leads to inaccurate stresses and displacements. The accuracy of the results increases with increasing the order of approximation.

## References

- [1] L. Tong, A. P. Mouritz, M. K. Bannister, 3D fibre reinforced polymer composites, Elsevier Science, Oxford, 2002.

- [2] A. P. Mouritz, M. K. Bannister, P. J. Falzon, K. H. Leong, Review of applications for advanced three-dimensional fibre textile composites, *Composites Part A: Applied Science and Manufacturing* 30 (12) (1999) 1445–1461.
- [3] Z. Ullah, L. Kaczmarczyk, C. Pearce, Three-dimensional nonlinear micro/meso-mechanical response of the fibre-reinforced polymer composites, *Composite Structures* 161 (2017) 204–214.
- [4] N. Dhanesh, S. Kapuria, G. G. S. Achary, Accurate prediction of three-dimensional free edge stress field in composite laminates using mixed-field multiterm extended Kantorovich method, *Acta Mechanica* 228 (8) (2017) 2895–2919.
- [5] C. Mittelstedt, W. Becker, Interlaminar stress concentrations in layered structures: Part I - A selective literature survey on the free-edge effect since 1967, *Journal of Composite Materials* 38 (12) (2004) 1037–1062.
- [6] A. Puppo, H. Evensen, Interlaminar shear in laminated composites under generalized plane stress, *Journal of Composite Materials* 4 (2) (1970) 204–220.
- [7] N. Pagano, R. B. Pipes, The influence of stacking sequence on laminate strength, *Journal of Composite Materials* 5 (1) (1971) 50–57.
- [8] J. Whitney, Free-edge effects in the characterization of composite materials, in: *Analysis of the test methods for high modulus fibers and composites*, ASTM International, 100 Barr Harbor Drive, PO Box C700, West Conshohocken, PA 19428-2959, 1973, pp. 167–167–14.
- [9] P. W. Hsu, C. T. Herakovich, Edge effects in angle-ply composite laminates, *Journal of Composite Materials* 11 (4) (1977) 422–428.
- [10] P. Bar-Yoseph, T. H. Pian, Calculation of interlaminar stress concentration in composite laminates, *Journal of Composite Materials* 15 (3) (1981) 225–239.
- [11] T. Kant, K. Swaminathan, Estimation of transverse/interlaminar stresses in laminated composites – a selective review and survey of current developments, *Composite Structures* 49 (1) (2000) 65–75.
- [12] C. Mittelstedt, W. Becker, Free-edge effects in composite laminates, *Applied Mechanics Reviews* 60 (5) (2007) 217–245.
- [13] R. B. Pipes, N. J. Pagano, *Interlaminar stresses in composite laminates under uniform axial extension*, Springer Netherlands, Dordrecht, 1994, pp. 234–245.
- [14] A. S. D. Wang, F. W. Crossman, Some new results on edge effect in symmetric composite laminates, *Journal of Composite Materials* 11 (1) (1977) 92–106.

- [15] J. Wei, J. Zhao, Three-dimensional finite element analysis on interlaminar stresses of symmetric laminates, *Computers & Structures* 41 (4) (1991) 561–567.
- [16] V.-T. Nguyen, J.-F. Caron, A new finite element for free edge effect analysis in laminated composites, *Computers & Structures* 84 (22-23) (2006) 1538–1546.
- [17] C. Fagiano, M. Abdalla, C. Kassapoglou, Z. Gürdal, Interlaminar stress recovery for three-dimensional finite elements, *Composites Science and Technology* 70 (3) (2010) 530–538.
- [18] O. Zienkiewicz, J. Zhu, The superconvergent patch recovery (SPR) and adaptive finite element refinement, *Computer Methods in Applied Mechanics and Engineering* 101 (1-3) (1992) 207–224.
- [19] R. Esquej, L. Castejon, M. Lizaranzu, M. Carrera, A. Miravete, R. Miralbes, A new finite element approach applied to the free edge effect on composite materials, *Composite Structures* 98 (2013) 121–129.
- [20] J. Espadas-Escalante, N. van Dijk, P. Isaksson, The effect of free-edges and layer shifting on intralaminar and interlaminar stresses in woven composites, *Composite Structures* 185 (2018) 212–220.
- [21] A. Solis, S. Sanchez-Saez, X. Martinez, E. Barbero-Pozuelo, Numerical analysis of interlaminar stresses in open-hole laminates under compression, *Composite Structures* 217 (2019) 89–99.
- [22] C. R. Cater, X. Xiao, R. K. Goldberg, X. Gong, Multiscale investigation of micro-scale stresses at composite laminate free edge, *Composite Structures* 189 (2018) 545–552.
- [23] K. Ballard, J. D. Whitcomb, Multiscale analysis of interlaminar stresses near a free-edge in a [45/0/90]<sub>s</sub> laminate, in: 2018 AIAA/ASCE/AHS/ASC Structures, Structural Dynamics, and Materials Conference, American Institute of Aeronautics and Astronautics, Reston, Virginia, 2018, p. 1707.
- [24] E. Carrera, A. Garcia de Miguel, G. A. Fiordilino, A. Pagani, Global/local analysis of free-edge stresses in composite laminates, in: AIAA Scitech 2019 Forum, American Institute of Aeronautics and Astronautics, Reston, Virginia, 2019, p. 1760.
- [25] A. Solis, S. Sánchez-Sáez, E. Barbero, Influence of ply orientation on free-edge effects in laminates subjected to in-plane loads, *Composites Part B: Engineering* 153 (2018) 149–158.
- [26] A. de Miguel, A. Pagani, E. Carrera, Free-edge stress fields in generic laminated composites via higher-order kinematics, *Composites Part B: Engineering* 168 (2019) 375–386.

- [27] S. Das, P. Choudhury, S. Halder, P. Sriram, Stress and free edge delamination analyses of delaminated composite structure using ANSYS, *Procedia Engineering* 64 (2013) 1364–1373.
- [28] V. Balasubramani, R. Nikhila, M. Alice Nila, Numerical prediction of interlaminar stresses in laminated composites, *IOP Conference Series: Materials Science and Engineering* 402 (1) (2018) 012121.
- [29] S. Dölling, S. Hell, W. Becker, Investigation of the laminate free-edge effect by means of the scaled boundary finite element method, *Proceedings in Applied Mathematics & Mechanics* 18 (1) (2018) e201800129.
- [30] R. Byron Pipes, J. Goodsell, A. Ritchey, J. Dustin, J. Gosse, Interlaminar stresses in composite laminates: Thermoelastic deformation, *Composites Science and Technology* 70 (11) (2010) 1605–1611.
- [31] M. Hajikazemi, W. Van Paepegem, A variational model for free-edge interlaminar stress analysis in general symmetric and thin-ply composite laminates, *Composite Structures* 184 (2018) 443–451.
- [32] M. Islam, P. Prabhakar, Modeling framework for free edge effects in laminates under thermo-mechanical loading, *Composites Part B: Engineering* 116 (2017) 89–98.
- [33] M. Ainsworth, J. Coyle, Hierarchic finite element bases on unstructured tetrahedral meshes, *International Journal for Numerical Methods in Engineering* 58 (14) (2003) 2103–2130.
- [34] M. Cortis, Numerical modelling of braided fibres for reinforced concrete, Ph.D. thesis, University of Glasgow (2016).
- [35] X. Meng, Numerical analysis of a fluid droplet subject to acoustic waves, Ph.D. thesis, University of Glasgow (2018).
- [36] P. Solin, K. Segeth, I. Dolezel, Higher-order finite element methods, Chapman & Hall/CRC, 2004.
- [37] L. Demkowicz, Computing with hp-adaptive finite elements, Chapman & Hall/CRC, 2007.
- [38] L. Kaczmarczyk, Z. Ullah, K. Lewandowski, X. Meng, X.-Y. Zhou, C. Pearce, [MoFEM \(Mesh Oriented Finite Element Method\)](#) (2019).  
URL <http://doi.org/10.5281/zenodo.438712>
- [39] S. Balay, W. D. Gropp, L. C. McInnes, B. F. Smith, Efficient management of parallelism in object oriented numerical software libraries, in: E. Arge, A. M. Bruaset, H. P. Langtangen

(Eds.), Modern Software Tools in Scientific Computing, Birkhäuser Press, 1997, pp. 163–202.

- [40] S. Balay, S. Abhyankar, M. Adams, J. Brown, P. Brune, K. Buschelman, L. Dalcin, A. Dener, V. Eijkhout, W. Gropp, D. Karpeyev, D. Kaushik, M. Knepley, D. May, L. C. McInnes, R. T. Mills, T. Munson, K. Rupp, P. Sanan, B. Smith, S. Zampini, H. Zhang, H. Zhang, [PETSc Users manual](#), Tech. Rep. ANL-95/11 - Revision 3.11, Argonne National Laboratory (2019).  
URL <https://www.mcs.anl.gov/petsc>
- [41] S. Balay, S. Abhyankar, M. Adams, J. Brown, P. Brune, K. Buschelman, L. Dalcin, A. Dener, V. Eijkhout, W. Gropp, D. Karpeyev, D. Kaushik, M. Knepley, D. May, L. C. McInnes, R. T. Mills, T. Munson, K. Rupp, P. Sanan, B. Smith, S. Zampini, H. Zhang, H. Zhang, [PETSc Web page](#) (2019).  
URL <https://www.mcs.anl.gov/petsc>
- [42] S. Abhyankar, J. Brown, E. M. Constantinescu, D. Ghosh, B. F. Smith, H. Zhang, PETSc/TS: A modern scalable ODE/DAE solver library, arXiv preprint arXiv:1806.01437 (2018).
- [43] T. J. Tautges, C. Ernst, C. Stimpson, R. J. Meyers, K. Merkley, MOAB: A Mesh-Oriented Database., Tech. rep., Sandia National Laboratories (2004).
- [44] Z. Ullah, Ł. Kaczmarczyk, S. Grammatikos, M. Evernden, C. Pearce, Multi-scale computational homogenisation to predict the long-term durability of composite structures, *Computers & Structures* 181 (2017) 21–31.
- [45] Z. Ullah, X.-Y. Zhou, Ł. Kaczmarczyk, E. Archer, A. McIlhagger, E. Harkin-Jones, A unified framework for the multi-scale computational homogenisation of 3D-textile composites, *Composites Part B: Engineering* 167 (2019) 582–598.
- [46] X.-Y. Zhou, P. Gosling, C. Pearce, Z. Ullah, Ł. Kaczmarczyk, Perturbation-based stochastic multi-scale computational homogenization method for woven textile composites, *International Journal of Solids and Structures* 80 (2016) 368–380.
- [47] Ł. Kaczmarczyk, Z. Ullah, C. J. Pearce, Energy consistent framework for continuously evolving 3D crack propagation, *Computer Methods in Applied Mechanics and Engineering* 324 (2017) 54–73.